Deformation processes of additively manufactured interstitial-strengthened high entropy alloy: In-situ high-energy synchrotron X-ray diffraction and microstructural appraisal

Wei Zhang [a], Jiajia Shen [c,d], J.P. Oliveira [c,d], Hui Wang [b], Shaochuan Feng [e], N. Schell [f], Bart J. Kooi [b], Yutao Pei [a,*]

[a] *Advanced Production Engineering, Engineering and Technology Institute Groningen, Faculty of Science and Engineering, University of Groningen, Nijenborgh 4, 9747 AG, the Netherlands*
[b] *Nanostructured Materials and Interfaces, Zernike Institute for Advanced Materials, Faculty of Science and Engineering, University of Groningen, Nijenborgh 4, 9747 AG, the Netherlands*
[c] *UNIDEMI, Department of Mechanical and Industrial Engineering, NOVA School Science and Technology, Universidade NOVA de Lisboa, Caparica 2829-516, Portugal*
[d] *CENIMAT/I3N, Department of Materials Science, NOVA School of Science and Technology, Universidade NOVA de Lisboa, 2829-516 Caparica, Portugal*
[e] *School of Mechanical Engineering, University of Science and Technology Beijing, Beijing 100083, China*
[f] *Institute of Materials Physics, Helmholtz-Zentrum Hereon, Max-Planck-Str. 1, Geesthacht D-21502, Germany*

ARTICLE INFO

ABSTRACT

Additively manufactured components often exhibit pronounced anisotropy due to the heterogeneous microstructure generated by the complex and repetitive thermal cycling history. Grain orientation is one of the determinant microstructural features that influences the activation of different deformation mechanisms. In this work, laser powder-bed fusion (LPBF) was applied to fabricate $Fe_{49.5}Mn_{30}Co_{10}Cr_{10}C_{0.5}$ interstitial-strengthened high entropy alloy (iHEA). Fabrication was performed at angles of 0° and 90° relative to the main laser scanning direction, and the plastic deformation behavior of these two oriented specimens was studied. The initial microstructure of the LPBF-built iHEA was composed of a complex heterogeneous columnar grains containing high-density dislocation network and a large number of stacking faults, as well as nano-precipitates and elemental segregation of Mn at subgrain boundaries. During uniaxial tension in-situ high-energy synchrotron X-ray diffraction (HE-SXRD) was performed to track the deformation processes and mechanisms of this metastable iHEA. The influence of different deformation mechanisms on the mechanical responses of the current LPBF-built iHEA was scrutinized combining in-situ HE-SXRD with electron backscattered diffraction (EBSD) and transmission electron microscopy (TEM) analyses, which not only gives insights into the macrostructural evolution but also provides comprehensive characterization on microstructural responses and the orientation-dependent effects imposed by the fabrication constraints originally imposed. The implemented multiscale characterization revealed the presence of a strain-induced fcc to hcp phase transformation, which is influenced by the growth texture close to <110> along the building direction. Moreover, EBSD and TEM analysis of the fracture regions uncovered the formation of nanosized deformation twins, confirming the simultaneous activation of phase transformation- and twinning-induced plasticity (TRIP and TWIP) effects. The results obtained in this work gain new insights into orientation-dependent deformation behavior of additively manufactured iHEA, which facilitates the microstructural design when exploiting the TRIP/TWIP effects.

1. Introduction

In recent years, high entropy alloys (HEAs), a novel alloy design strategy consisting of at least five principle elements, have received increasing research attention as a result of their broad compositional space and superior properties on various fronts, especially the extraordinary combination of strength and ductility in mechanical response in broad temperature ranges [1,2]. Among the main HEAs systems studied,

---

* Corresponding author.
E-mail address: y.pei@rug.nl (Y. Pei).

the interstitial-strengthened $Fe_{49.5}Mn_{30}Co_{10}Cr_{10}C_{0.5}$ HEA (iHEA) has aroused ever-growing attention due to its multiple microscopic deformation mechanisms [3–5]. Specifically, it has been reported that this fcc/hcp dual-phase iHEA can simultaneously exhibit different deformation mechanisms including dislocation slip, nano twinning- and phase transformation-induced plasticity (TWIP and TRIP, respectively) during plastic deformation, resulting in an outstanding strength-ductility combination [5]. During TWIP and TRIP, the formation of twinning and phase interfaces creates effective barriers for the movement of dislocations, leading to a dynamic Hall-Petch effect, which contributes to the steady work hardening rate and delays necking failure [6–8]. The high density of twins and phase transformation behavior originate from the low stacking fault energy (SFE) in this $Fe_{49.5}Mn_{30}Co_{10}Cr_{10}C_{0.5}$ iHEA, which depends on chemical composition and deformation temperature [9]. Additionally, phase transformation and nano-twinning behavior have been found to correlate with the orientational relationship between the overall grain orientation and the loading direction [10], suggesting the possibility for tailoring the mechanical properties through the manipulation of the preferential crystallographic texture during a given manufacturing process.

In the $Fe_{49.5}Mn_{30}Co_{10}Cr_{10}C_{0.5}$ iHEA manufactured by traditional methods including casting and subsequent thermomechanical treatment, microstructures with specific grain size distributions are generally favored, such as heterogeneous and bimodal grain structures [11,12]. Additional deformation accommodation capabilities can be provided through the introduction of storage dislocations, stacking faults, deformation twins, as well as Lomer-Cottrell (L-C) locks, thereby resolving the long-standing strength-ductility trade-off problem. The conventional manufacturing methods employed previously contributed greatly to the comprehensive understanding of this $Fe_{49.5}Mn_{30}Co_{10}Cr_{10}C_{0.5}$ iHEA. However, from an industrial point of view the adoption of iHEAs cannot be restricted to the relatively simple geometries as those enabled by conventional manufacturing routes.

Additive manufacturing (AM), also known as 3D printing, is widely acknowledged as a technique for building parts layer by layer with minimal material loss when compared to traditional subtractive manufacturing methods [13]. Based on a computer-aided design model, this layer-by-layer process allows the fabrication of near-net-shaped metallic components with complex geometries [14]. Laser powder-bed fusion (LPBF) is a laser-based AM method that uses a high-energy laser to melt the raw material powder, which is previously spread on a substrate [13–15]. The LPBF process is suitable for the fabrication of metal-based materials including HEAs [2,5,10]. During LPBF, the thermal history experienced by the materials involves a steep directional temperature gradient along the building direction. This results in strongly textured coarse columnar grains along the building direction, which can lead to anisotropic mechanical behavior of the fabricated components [16]. Therefore, it is necessary to gain a thorough understanding of the deformation processes and mechanisms governing these mechanical responses, which will allow for the development of predictive approaches to facilitate further applications of AM techniques.

Nowadays, time-resolved high-energy synchrotron X-ray diffraction (HE-SXRD) provides unique insights into the deformation processes, which is fundamental to better understand the competition between different deformation mechanisms including dislocation slip, deformation twinning, and phase transformation. Combined with the use of 2D detectors, the high penetration enabled by the use of high-energy photons allows for a fast acquisition of the full Debye-Scheler rings capturing bulk microstructure information in a single beam shot under one second, which is very suitable for studying thermal and/or mechanical loading processes of metallic materials [17–19].

In the present work, tensile specimens of $Fe_{49.5}Mn_{30}Co_{10}Cr_{10}C_{0.5}$ alloy were fabricated by LPBF under two conditions: 0° and 90° relative to the main laser scanning direction. During tensile deformation, HE-SXRD and electron backscattered diffraction (EBSD) techniques were employed separately to in-situ detect the mechanical response and

microstructural evolution of this additively manufactured iHEA, aiming to determine the activation sequence of the bulk deformation mechanisms and their correlation with the textures obtained in LPBF-fabricated iHEA. The analytical approaches employed here allow a continuous tracking of the deformation processes, providing clear evidence of the contribution of different deformation mechanisms related to crystallographic orientations. These studies are complemented by complementary microstructural analysis including EBSD and transmission electron microscopy (TEM), aiming at elucidating the deformation mechanisms and accelerating the fabrication and development of high-performance HEAs.

2. Materials and methods

2.1. Material preparation

Pre-alloyed $Fe_{49.5}Mn_{30}Co_{10}Cr_{10}C_{0.5}$ iHEA powder with a particle size distribution from 15 to 53 μm was utilized in this study. The applied LPBF system was SLM 125HL (SLM Solutions Group AG, Lübeck, Germany). The preheating temperature of the build platform was set to 180 °C. Tensile specimens were fabricated directly on the stainless steel substrate with the process parameters set as follows: laser power of 300 W, scanning speed of 700 mm/s, hatch distance of 120 μm and layer thickness of 30 μm. These optimized parameters take into account both bulk density and mechanical properties. The volumetric energy density was calculated to be 119 J/mm³. A scanning strategy with 90° limitation angle and a 33° rotation angle between every two successive layers was applied, aiming at generating different grain orientations on the build plane. The tensile specimens were printed with the longitudinal tensile axis at 0° and 90° with respect to the main laser scanning direction (X), respectively. The as-printed specimens are shown in Fig. 1a. The coordinate symbols X-Y-Z used in Fig. 1a represent the main laser scanning direction, transverse direction and building direction, respectively. After the LPBF process, 1.2 mm thick tensile specimens were sliced by electrical discharge machining, then ground and polished for further characterization. The detailed dimensions of the tensile specimens are depicted in Fig. 1b, with the gauge section of 11 mm in length, 3 mm in width and 1.2 mm in thickness.

2.2. Microstructure characterization and mechanical testing

For microstructural characterization, EBSD maps were acquired on different planes around the gauge center of the as-printed specimen to examine the grain structure, crystallographic orientation and phase
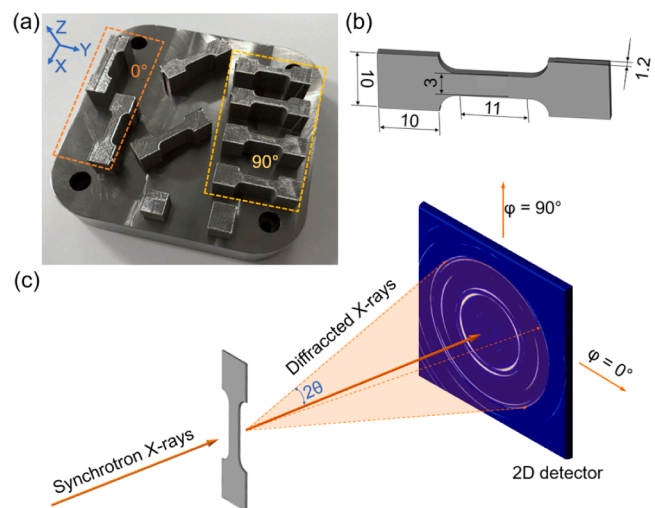

Fig. 1. (a) As-printed iHEA specimens, (b) dimensions of the tensile specimens (mm), (c) representation of the setup for the HE-SXRD experiments.

constituents. TEM (JEOL 2200FS operating at 200 kV) and scanning TEM (STEM, FEI Thermo Helios G4 CX operating at 30 kV) were applied to analyze the subgrain morphology and dislocation networks. Ex-situ uniaxial tensile tests were conducted on the polished tensile specimens using a Kammrath-Weiss tensile module with a strain rate of 3×10^{-4} s^{-1} at room temperature. Three specimens of each condition were tested to ensure repeatability and data reliability. Micrographs were collected near the fractured surfaces by EBSD and TEM to analyze the deformation and strengthening mechanisms.

2.3. In-situ HE-SXRD and EBSD tensile tests

In-situ HE-SXRD was employed during uniaxial tensile tests for each condition in transmission mode at beamline P07-HEMS of PETRA III (Deutsches Elektronen-Synchrotron, DESY, Hamburg, Germany), with a wavelength of 0.14253 Å, to observe the microstructural evolution with high spatial and temporal resolution. A 2D PerkinElmer fast detector was applied for acquisition of the Debye-Scherrer diffraction rings. The incident X-ray beam was positioned at the center of the specimens before and during tensile tests. A representation of the HE-SXRD experiment setup is shown in Fig. 1c. The slit-aperture size of the beam was 0.5×0.5 mm². The acquired data was processed using Fit2D and MAUD software. Peak fitting was applied to determine the deformation microstructure of the additively manufactured iHEAs. The post-processed 2D patterns were converted into one dimensional intensity versus diffraction angle plots via full azimuthal integration. For reference, the azimuthal angle, φ, is defined in Fig. 1c. MAUD software was employed for quantitative analysis of different phases by the Rietveld method. In addition, in-situ EBSD analysis was also performed on the gauge center of the specimens during the tensile tests to further inspect the microstructural evolution.

3. Results and discussions

3.1. As-printed microstructure

Representative EBSD scans of the two types of undeformed specimens are shown in Fig. 2. Columnar grains with obvious preferred orientations were observed in both specimens. The gradual change in color within individual columnar grains in the inverse pole figures (IPFs) (Figs. 2a and 2d) indicates the existence of abundant subgrain structures with low angle grain boundaries. Such microstructural characteristics are typical of LPBF-processed metallic materials and result from the rapid cooling of the molten metal during solidification [10,20]. Furthermore, there is a slight difference in the grain shape of the two specimens, which is considered to be due to different solidification rates during laser scanning despite the same process parameters. That is, the laser scanning of the 0° specimen is approximately along the gauge length direction, while that of the 90° specimen is along the width direction of the gauge section, leading to more heat accumulation in the former and thus relatively slower solidification rate, which in turn promotes the formation of coarser grains in the 0° specimen. The phase maps of the as-printed specimens (Figs. 2b and 2e) reveal the presence of a dominant fcc structure with trace amounts of hcp phase. The control of chemical composition, SFE and processing parameters has been reported to be highly important for determining the fractions of fcc and hcp phases generated, as well as the resulting mechanical performance of additively manufactured dual-phase fcc/hcp HEAs [5,21–24]. For the current applied iHEA, the low-temperature and high-temperature phases are referred to as hcp and fcc, respectively. Fast cooling during the LPBF process suppresses the thermally induced martensitic transformation and allows the preservation of fcc phase as a metastable phase at room temperature, which could transform into hcp phase through a strain-induced phase transformation mechanism at room temperature [5,10], which will be analyzed in detail in this work.

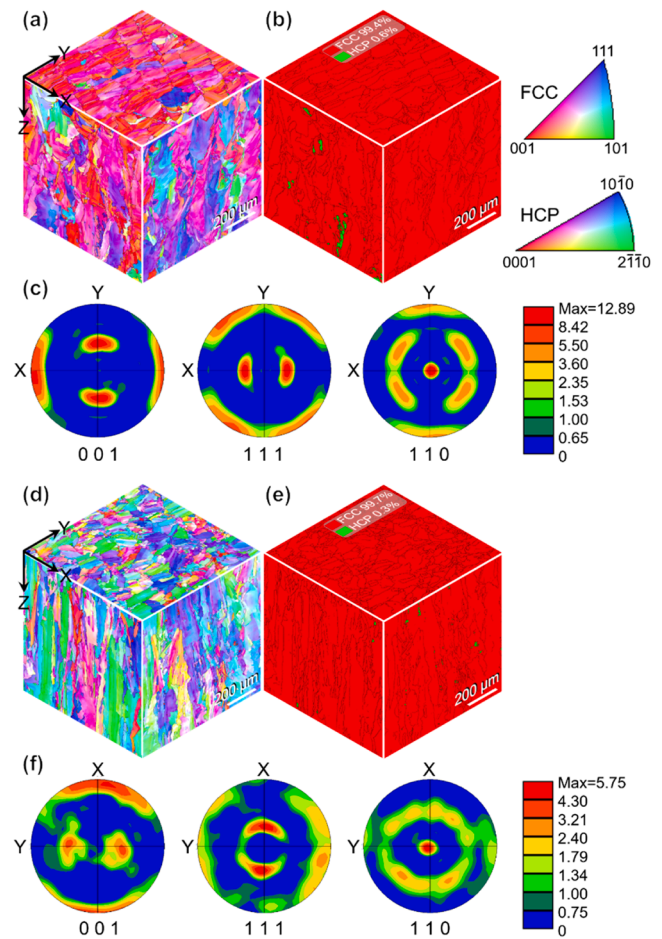According to the pole figures (PFs) in Fig. 2c and 2f, a similar near

Fig. 2. EBSD scans on different planes of the additively manufactured iHEAs. (a) IPF// tensile direction (X), (b) phase maps and (c) PFs of the 0° specimen; (d) IPF// tensile direction (Y), (e) phase maps and (f) PFs of the 90° specimen.

<110> growth texture aligned with the building direction (Z) could be observed for both specimens, and a near <001> growth texture along the main laser scanning direction (X) could also be detected. Fcc grains tend to grow along the <001> direction with respect to the maximum temperature gradient [24–26]. During the LPBF process, the shape of the molten pool is often elliptical, and the thermal gradient is along the direction from the boundary of the molten pool to its center. Therefore, most of the grains grew oriented by 45° with the building direction, resulting in the formation of <110> oriented grains along the building direction. On the other hand, as the laser beam advances in a specific direction (X in this study), a temperature gradient along the front to back of the molten pool is also formed, resulting in a near <001> crystallographic orientation parallel to the main laser scanning direction. For the 0° and 90° specimens studied in the present work, it could be noticed that the maximum intensity of the PFs varies greatly, with the 0º specimen showing a more pronounced preferred orientation. This is considered to be related to the process characteristics of LPBF, where the interaction of the gas flow direction with the laser scanning direction affects the grain growth orientation, and the specific mechanism needs to be further systematically studied. The relatively high multiples of uniform density indicate a less smooth granular orientation distribution, which would yield more pronounced anisotropy in the X-Y plane, e.g. for the 0° specimens, the dominant grain orientation along the tensile direction (X) is near <001>, while for the 90° specimens, mainly near <111> and <110>. The 33° scanning strategy with a 90° limitation angle applied in this study is considered to be the dominant factor for generating anisotropy in the X-Y plane.

To precisely determine the existing phases and the corresponding phase fractions, HE-SXRD was applied in the X-Y plane of the two types of specimens. The obtained 2D diffraction rings have been integrated into diffraction patterns, and the results are detailed in Fig. 3. In addition to the fcc and hcp phases observed by EBSD, $M_{23}C_6$- and M_7C_3-type precipitates were also detected, which is attributed to the excellent signal-to-noise ratio of synchrotron X-ray sources enabling phase identification and quantification of even minority phases. According to the Rietveld refinement, the phase fractions of fcc, hcp, $M_{23}C_6$ and M_7C_3 for the undeformed 0° specimens are calculated as 96.0 %, 1.8 %, 1.4 % and 0.8 %, respectively. The corresponding phase fractions of the 90° specimens are 95.1 %, 2.3 %, 1.8 % and 0.8 %, respectively. It should be noted that the phase fractions of these two orientated specimens show no obvious difference, as expected.

A bright-field STEM image of the LPBF-printed specimens prior to the tensile deformation is shown in Fig. 4a. There is a clear fringe contrast from pre-existing stacking faults (SFs) and their intersections. Most fringes terminated at the boundaries of subgrains. Fig. 4b is a high-resolution TEM (HRTEM) image of the SFs, and the inset reveals the fcc phase structure. The current iHEA has a low SFE [11,22] and is susceptible to the formation of SFs. Additionally, highly entangled dislocations separating columnar subgrains could also be observed, as indicated by yellow arrows in Fig. 4a. During the LPBF process, the extremely fast temperature drop suppressed the grain growth after solidification, resulting in the generation of a large number of nanoscale columnar subgrains. It is expected that abundant geometrically necessary dislocations (GNDs) should generate to compromise the stress/energy induced by the low misorientation between adjacent subgrains [24,27,28]. As a result, the dense GNDs developed into thick dislocation walls around the subgrain boundaries and progressively into high-density dislocation networks [29], which is beneficial to promote dislocation strengthening through blocking the movement of dislocations during deformation. Considering ductility, however, a high density of pre-existing dislocations may decrease the overall elongation by consuming available dislocation capacity. On the other hand, the dislocation networks would contribute to the steady work hardening through partially inhibiting dislocation movement, thereby promoting elongation [29,30]. These opposing views still need to be confronted in a deeper exploration of the LPBF process. Furthermore, the high initial defect density (SFs and dislocations) in the current LPBF-built iHEA specimens would lead to an earlier onset of phase transformation during deformation, which will be discussed in the mechanical property analysis section.

The dark-field STEM image in Fig. 4c clearly presents non-negligible nanoscale precipitates with nearly spherical shape, which is consistent with the precipitate phases previously detected by HE-SXRD, implying the potential for significant precipitation strengthening. To further clarify the elemental composition, energy dispersive X-ray (EDX) analysis was performed under STEM mode, and the results are shown in Fig. 4d. In addition to the uniform distribution of C element in these precipitates, the local enrichment of O and S elements can be observed, which is related to the contamination during the powder fabrication process [31]. Fig. S1 in the supporting information shows the element distribution of a single precipitated particle, where a clearer interstitial element distribution can be observed. In addition, an obvious enrichment of Mn solute atoms can also be observed at the subgrain boundaries (including precipitates), indicating that the precipitates are a mixture of Mn-rich oxide, sulfide and carbide. The segregation of Mn along the subgrain boundaries is believed to promote both dislocation density, twinning and/or second phase nucleation in addition to the strengthening effect [29,30]. Both precipitation and segregation are frequently reported in LPBF-fabricated alloys [24,28–30,32]. For example, the precipitation of Cr-rich carbide has been reported for 1 % C-CoCrFeMnNi HEA [24] and $CoCrFeNiC_{0.05}$ HEA [33]. In this case, elemental Cr is rapidly diffused to the grain boundaries and forms Cr-rich $M_{23}C_6$ carbides due to its high affinity with interstitial C [34]. On the other hand, as the material is repeatedly heated and cooled during the LPBF process, it may be frequently exposed to the sensitization temperature range for Cr-rich carbide formation, resulting in carbide generation [24,33,34]. For elemental segregation, due to the rapid melting and solidification of multi-element alloys, the supercooling at the solidification front under a large temperature gradient would lead to a pronounced concentration gradient, allowing elements with larger diffusion coefficients to precipitate near the grain boundaries, as it also occurs to Mn in high Mn TWIP steels [32], Cr and Mn in CoCrFeMnNi HEA [28], Cr and Mo in 316 L stainless steel as ferrite stabilizers [29], and even introducing Cottrell atmosphere to stabilize dislocation walls [30].

3.2. In-situ tensile testing and microstructural evolution

Uniaxial tensile tests were performed at room temperature. The engineering stress-strain curves and strain hardening rate curves for the two types of specimens are presented in Fig. 5. The mechanical properties are summarized in the insert table. The 90° specimen exhibited higher yield strength and ultimate tensile strength (UTS) with reduced elongation compared to the 0° specimens. Notably, along with the LPBF process for full design freedom of fabrication, competitive yield strength and UTS of the as-printed parts were successfully achieved with reasonable total elongation when compared to conventionally casted and heat-treated iHEA (σ_y: ~520 MPa, UTS: ~950 MPa, e_f: ~60 % [11]; σ_y: 225 MPa, UTS: 655 MPa, e_f: 38 % [35]). As shown in Fig. 5b, from the end of the elastic deformation stage, a near-horizontal stable
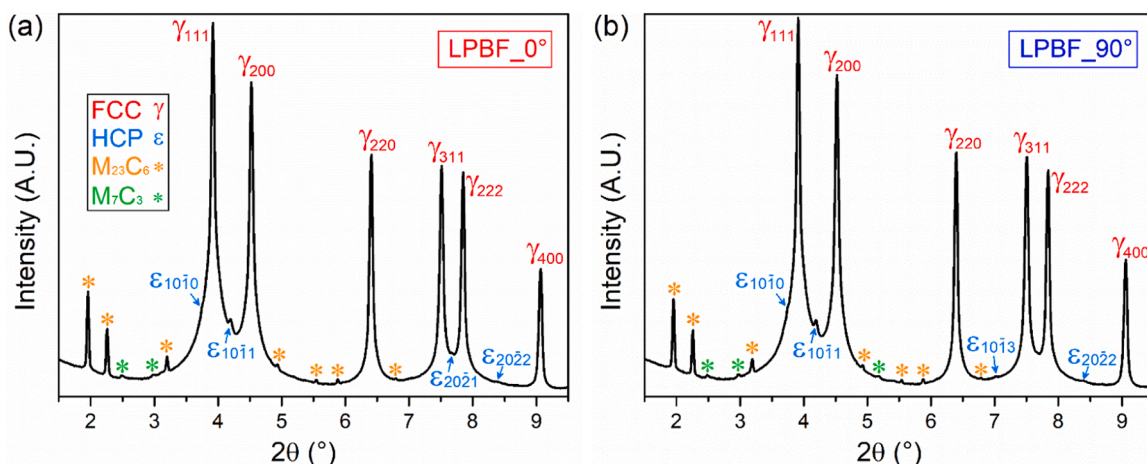

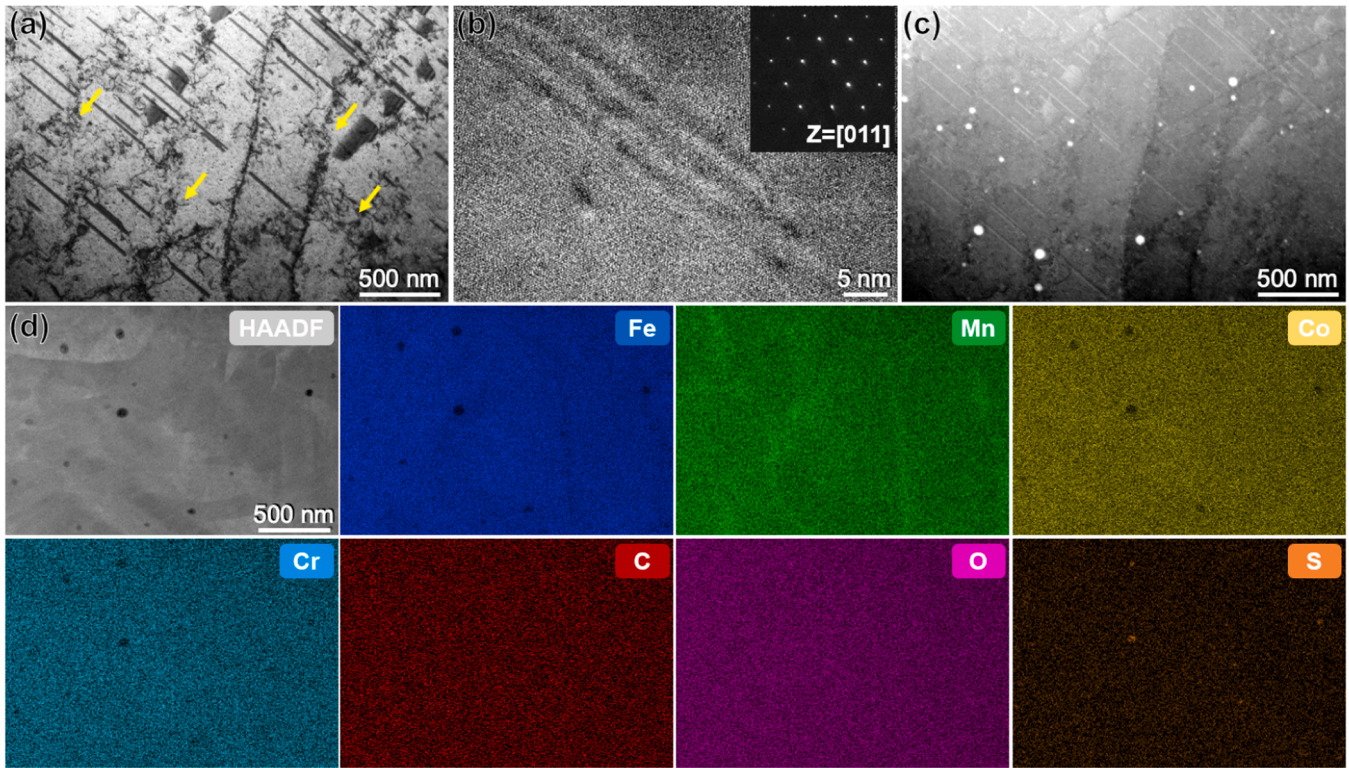**Fig. 3.** HE-SXRD pattern of LPBF-built 0° specimen (a) and 90° specimen (b).

Fig. 4. (a) Bright-field STEM micrograph showing stacking faults in undeformed specimen with the yellow arrows pointing to highly entangled dislocations separating columnar subgrains, (b) HRTEM image of the stacking fault, (c) dark-field STEM image showing precipitates, (d) EDX mappings of both substitutional (Fe, Mn, Co, Cr) and interstitial (C, O, S) elements for the subgrain boundaries and precipitates.
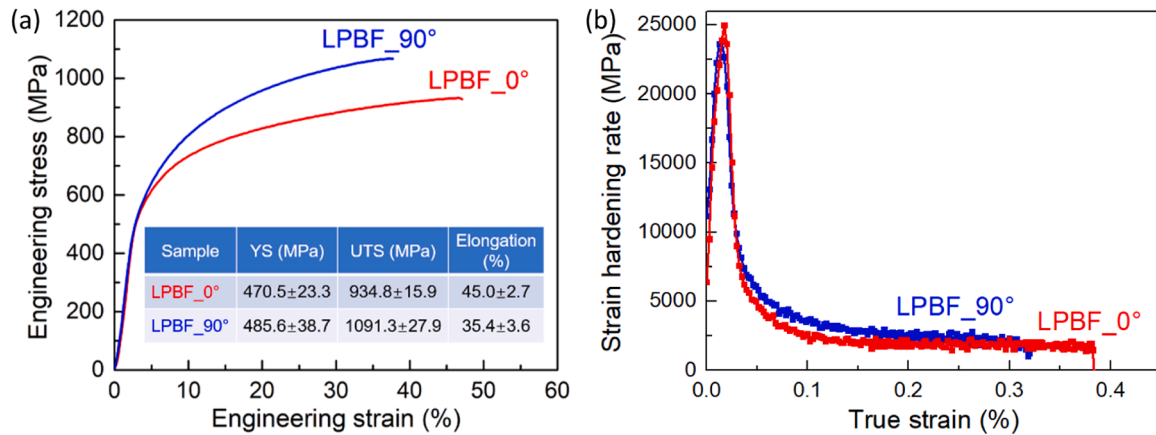

Fig. 5. (a) Representative tensile stress-strain curves and (b) strain hardening curves of the LPBF-built iHEAs.

hardening response was observed until fracture, with no evidence of secondary hardening, indicating a continuous and steady strain hardening process during tensile deformation. The 90° specimen shows a slightly higher strain hardening rate than the 0° specimen. For the currently studied iHEA, it has been reported that mechanical twinning and phase transformation are considered essential in the later deformation stages, which occur following dissolved partial dislocations and slip [5,11]. Upon reaching a critical stress or strain, twins and the second hcp phase will nucleate and expand, contributing to a continuous and steady strain hardening and preventing early necking through providing additional barriers for movement of dislocations.

3.2.1. In-situ HE-SXRD analysis

To quantitatively analyze the deformation process of the iHEA

specimens fabricated with different orientations relative to the loading direction, in-situ HE-SXRD tensile testing was conducted at room temperature to precisely determine the evolution of grain orientation and phase transformation, with a schematic diagram shown in Fig. 1c. Synchrotron radiation characterization technique has been applied in various studies for lattice strain calculations, dislocation analysis, phase identification and phase transformation behavior of TRIP, TWIP steels and HEAs [14,17,20,36–38]. Fig. 6 shows the evolution of different diffraction peaks for the 0° and 90° specimens during the whole deformation process. To have a clear view of different peaks, here the intensity data was used in logarithmic scale instead of absolute values. It can be observed that as the strain increases, the intensity of fcc diffraction peaks decreased gradually, while that of the hcp phase significantly increased. The peaks of $M_{23}C_6$- and M_7C_3-type carbides
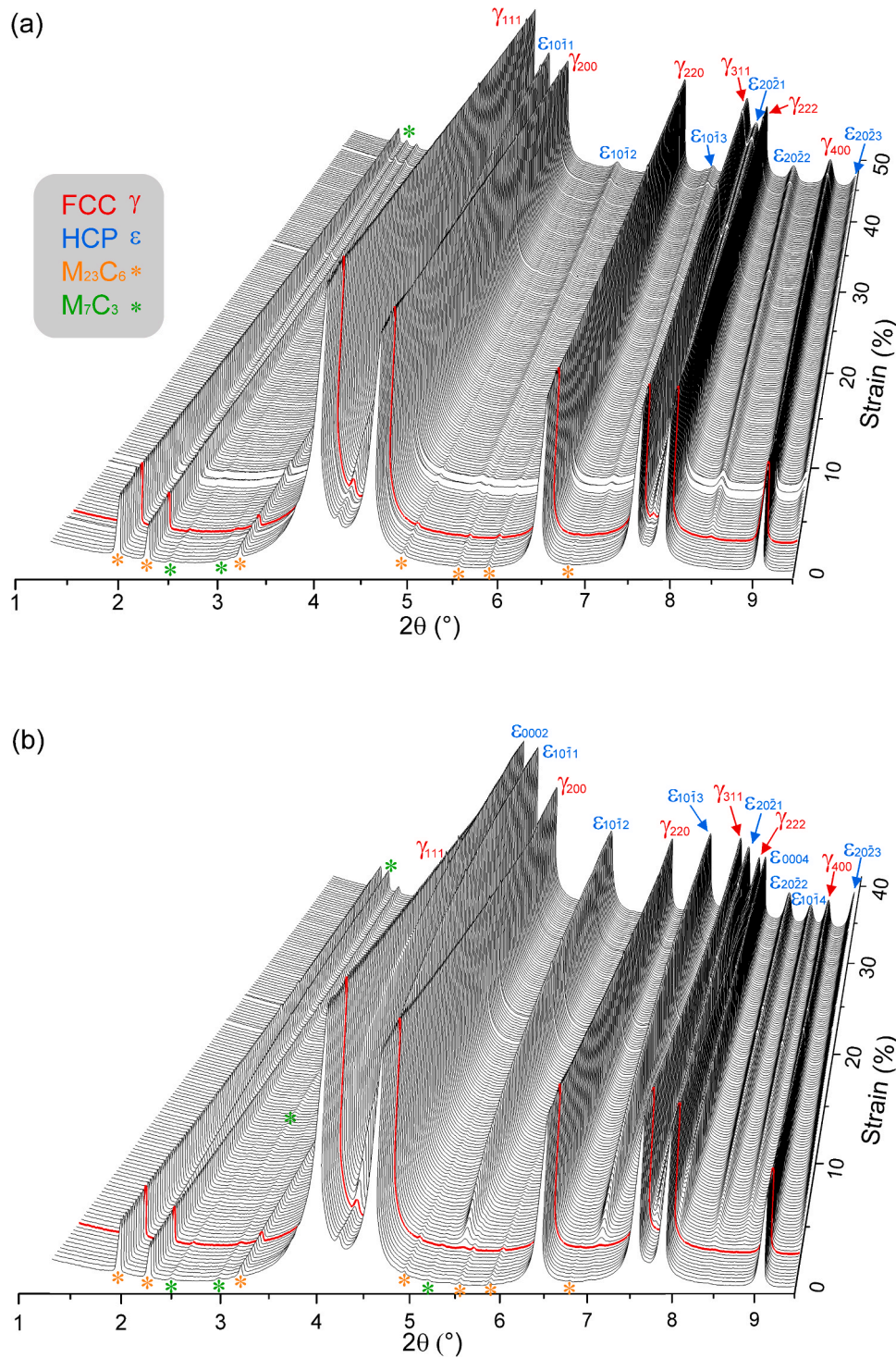
Fig. 6. Series of HE-SXRD patterns during tensile deformation of LPBF-built 0° specimen (a) and 90° specimen (b).

show no significant change during deformation except for a slight reorientation of the M_7C_3-type carbides. Specifically, before loading, the following fcc and hcp reflections are present: $(111)\gamma$, $(200)\gamma$, $(220)\gamma$, $(311)\gamma$, $(222)\gamma$, $(400)\gamma$ and $(10\bar{1}1)\varepsilon$, $(10\bar{1}3)\varepsilon$, $(20\bar{2}1)\varepsilon$, $(20\bar{2}2)\varepsilon$. When the strain reaches ~2.5 % (marked with the red diffraction line), the $(10\bar{1}1)\varepsilon$, $(10\bar{1}2)\varepsilon$, $(10\bar{1}3)\varepsilon$, $(20\bar{2}1)\varepsilon$, and $(20\bar{2}2)\varepsilon$ reflection intensities start to increase, representing the initiation of the fcc to hcp phase transformation. Afterwards, the intensity of these reflections significantly increases with strain until final fracture.

The strain-induced martensitic transformation occurs through the change of the atomic stacking sequence from the ABCABC type of fcc phase to the ABAB type of hcp phase, which introduces SFs on every second {111} fcc plane [39]. This phase transformation strongly depends on the SFE of the material. In general, as the SFE of a specific alloy decreases, the deformation mechanisms will shift from dislocation slip, to mechanical twinning, and finally to phase transformation, where SFs are the nucleation sites for twining and/or hcp phase formation [40,41]. SFs are more easily induced with increasing strain due to the minimized bulk free energy and the total SFE, leading to a higher work hardening rate [42]. The current LPBF-built iHEA has higher initial defect densities

(SFs and dislocations) due to its lower SFE, contributing to a higher level of lattice stress in the fcc matrix [43], which would bring about an earlier onset of the phase transformation and/or twin formation during tensile deformation. The coupled effect of martensitic phase transformation and deformation twinning occurring in the metastable fcc HEA would contribute to enhanced strain hardening and excellent mechanical properties. During this process, TWIP/TRIP effects provide an improved plasticity, which is also observed in manganese and austenitic stainless steels [17,44].

From the azimuthal-2θ intensity evolution maps at different strain levels shown in Fig. 7, it can be observed that, for both specimens, no obvious twinning was formed on the (111) and (100) fcc planes during deformation, except for the decrease of diffraction intensity. Nevertheless, grain orientation-dependent deformation mechanisms can still be observed, which are detailed in the intensity evolution associated with specific planes within the selected 2θ range. Prior to deformation (0 % strain), the dispersed lines of the fcc phase along the azimuth angle represent that the grains are oriented in specific preferred directions. Specifically, the (200) plane of the 0° specimen exhibits strong intensity at azimuthal angles of 90° and 270°, corresponding to the tensile loading direction (Fig. 1c), while the 90° specimen exhibits a strong orientation of (111) plane parallel to the loading direction and (200) plane perpendicular to the loading direction, consistent with the IPF results

shown in Fig. 2. Thereafter, tensile deformation resulted in the formation of distinct hcp phase and slip-driven grain rotations, where the latter is observable from a gradual shift in the diffracted intensity along the azimuthal angle towards preferred orientations (see white arrows). This slip-driven grain rotation is more clearly observed in the 90° specimen. For the 0° specimen, the deformation-induced hcp phase is mainly formed along the (10$\bar{1}$1) plane near the tensile direction (90° and 270° azimuth angle). For the 90° specimen, the (0002) and (10$\bar{1}$1) planes of the hcp phase show similar azimuthal intensities, that is, parallel to the (111) plane of the fcc phase along the tensile direction, indicating a specific orientation relationship between these two phases. These results confirm the dependence of the deformation mechanisms on the grain orientation of additively manufactured HEAs.

The quantitative evolution of the volume fractions of fcc, hcp and two carbide precipitates obtained through Rietveld analysis is presented as a function of strain in Fig. 8. The onset of the fcc to hcp phase transformation occurred at a strain of ~2.5 % in both specimens (Fig. 6). Below this strain, the potentially nucleated hcp phase constitutes a significant fraction of the shear bands, as hcp phase results from the shear-band formation by regular overlapping of SFs [17,39,45]. At the strains above this, however, this contribution becomes less relevant. During plastic deformation between 2.5 % and 10 % strain, the hcp phase fractions increase from 1.8 % and 2.3 % to 5.0 % and 5.7 % in the
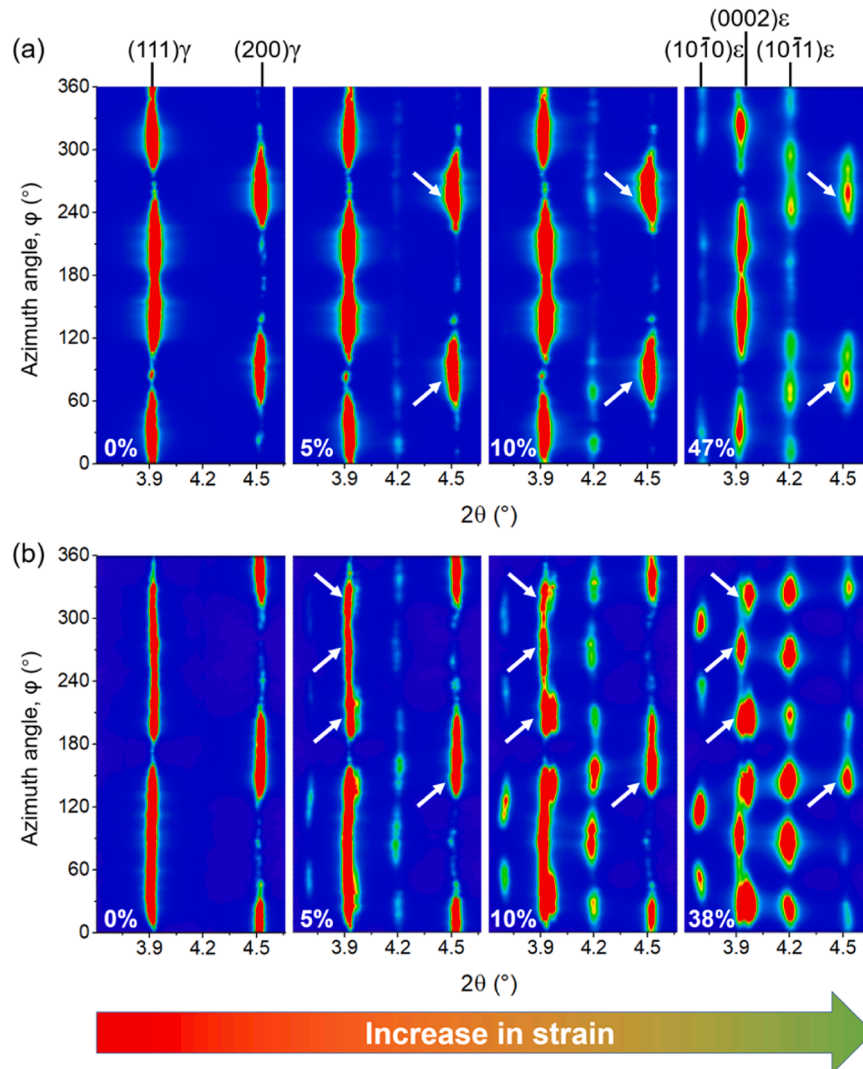

Fig. 7. HE-SXRD azimuthal angle-2θ intensity map revealing strain-induced fcc-hcp phase transformation and grain orientation evolution during tensile deformation of (a) 0° specimen and (b) 90° specimen.
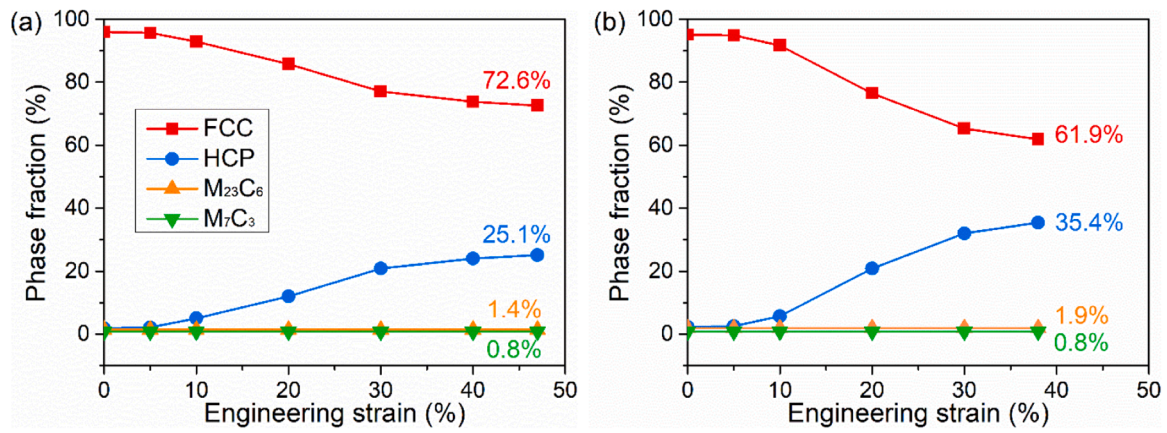
Fig. 8. Relative phase fractions during tensile deformation of (a) 0° specimen and (b) 90° specimen.
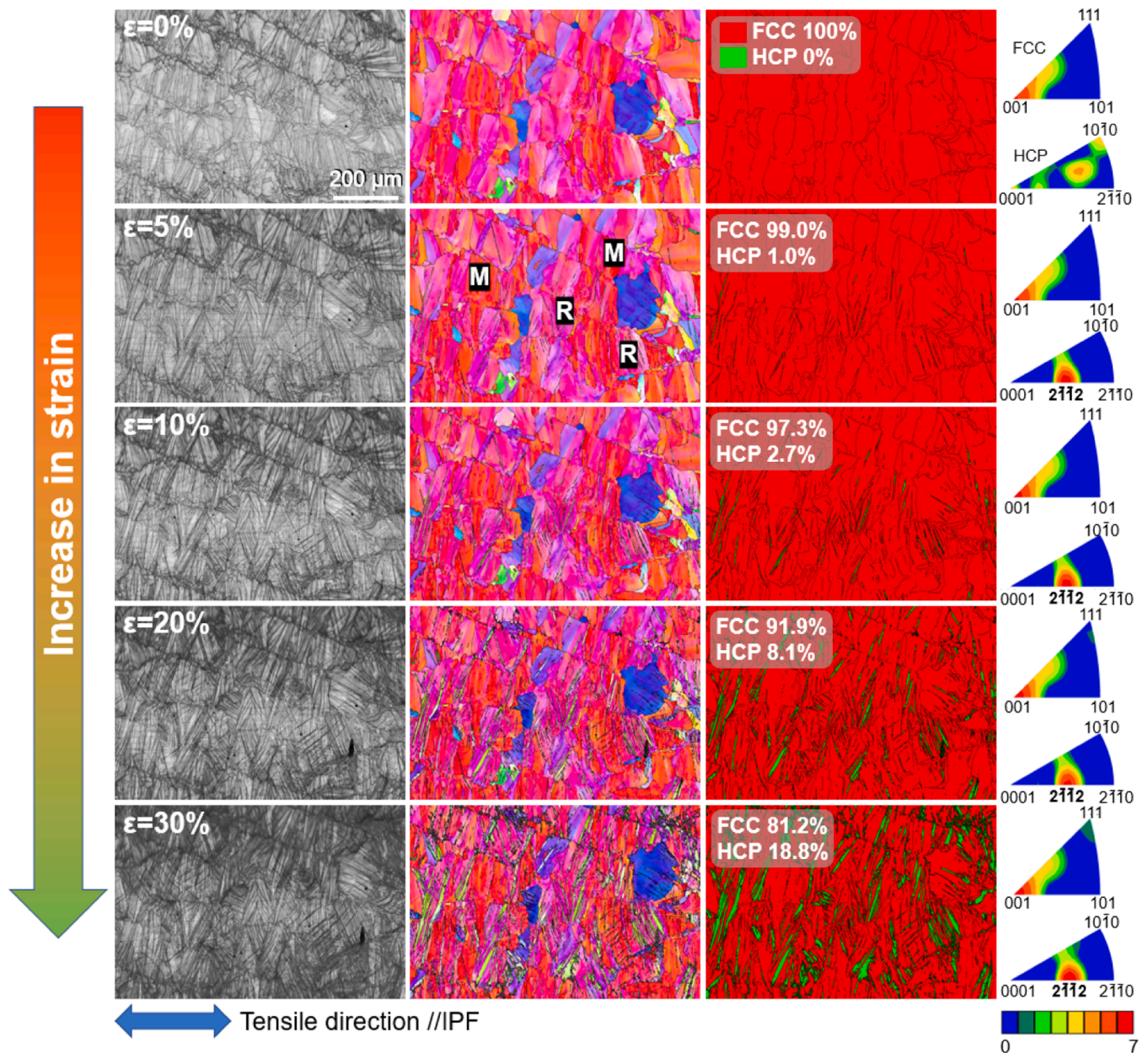

Fig. 9. In-situ EBSD results during deformation of the 0° specimen.

0° and 90° specimens, respectively. Afterwards, the volume fractions of hcp phase increase rapidly with increasing strain, reaching 20.8 % and 32.0 %, respectively, at 30 % engineering strain. At plastic deformations above this, the increase rate of the volume fraction of hcp phase slows down, especially for the 0° specimen where the hcp remains relatively stable after 40 % strain. The volume fraction of hcp phase for the 0° and 90° specimens reached 25.1 % and 35.4 % respectively upon material failure. Also, a simultaneous decrease of fcc phase can be observed during the whole plastic deformation process. The steady strain hardening shown in Fig. 5b is the result of hcp phase formation at the onset of plastic deformation. The strain hardening behavior, which reflects the plastic deformation capacity of the material under different deformation states, can be interpreted as a measure of the interaction between dislocations and obstacles [42,46]. The observed slightly higher strain hardening of the 90° specimen compared to the 0° specimen is attributed to the formation of more hcp/fcc interfaces in the former, which increases the dislocations pile-up in the 90° specimen and contributes to the higher tensile strength, consistent with the tensile results in Fig. 5b.

The phase evolution with strain presented in Fig. 8 is comparable to those reported for the metastable 16Cr-7Mn-9Ni austenitic steel [43] and Co-28Cr-6Mo alloy [42]. For the latter, the fcc to hcp phase transformation starts near zero strain and demonstrates grain orientation-dependent phase transformation behavior. Additionally, due to the different elastic properties of fcc and hcp, the formation of martensite is also related to the presence of residual stress [42,47], which is easily generated during non-equilibrium thermal cycling associated to the LPBF process. Therefore, the phase transformation process of LPBF-built specimens can be triggered at a lower macroscopic strain.

3.2.2. In-situ EBSD analysis

The microstructural changes during tensile deformation were analyzed by in-situ EBSD, and the evolution of strain-induced fcc to hcp phase transformation, grain size and morphology were detected. The results of the 0° and 90° specimens are shown in Fig. 9 and Fig. 10, respectively. It is worth mentioning that when using EBSD, limited
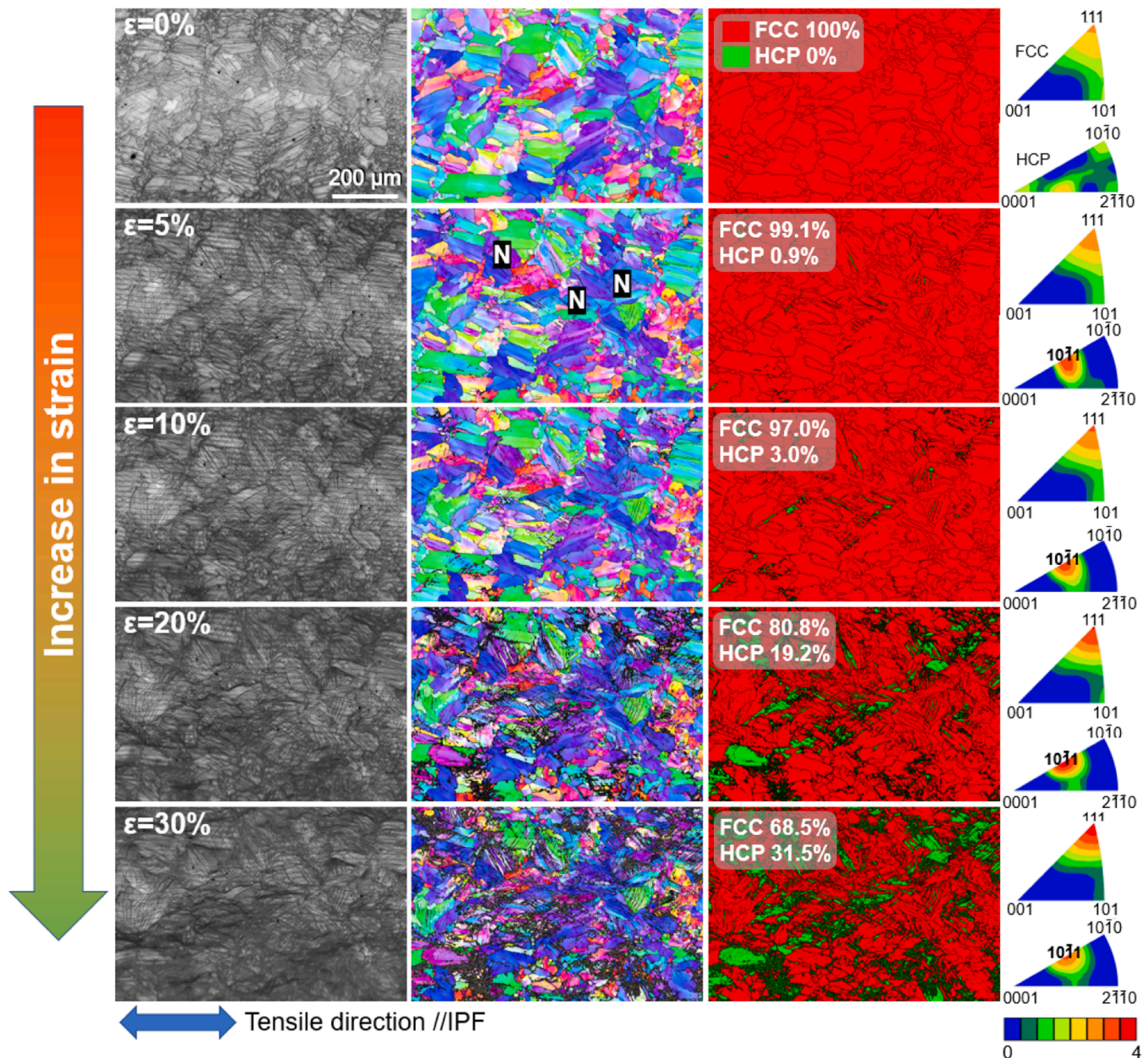

Fig. 10. In-situ EBSD results during deformation of the 90° specimen.

detection of fine hcp grains and a smaller volume fraction of this phase may be expected due to its limited resolution. At 30 % strain, the volume fraction of the hcp phase in the 0° specimen is lower than that of the 90° specimen, consistent with the previously shown HE-SXRD results. One major factor that justifies this is that the near <100> growth texture parallel to the tensile direction in the former inhibited the hcp phase nucleation. It has been reported that the correlation between individual crystallographic orientation and the direction of macroscopic uniaxial tension strongly dominates the twinning and phase transformation behavior of alloys with low SFE [10,48–50]. Through a combination of experiments and modeling, Slone et al. [49] and Uzer et al. [50] concluded that grains with an initial orientation of <100> parallel to the loading direction are more likely to deform by gliding rather than twinning or phase transformation even at large strains, while grains with <111> parallel to the loading direction have the greatest propensity for twinning and phase transformation. Likewise, grains with intermediate orientations such as <110> would respond intermediately. Similar results can also be observed from the EBSD results during deformation. As shown in Fig. 9, from the IPF of the 0° specimen with 5 % strain, the grains marked with R with orientations close to <112> parallel to the tensile direction tend to transform into lamella hcp phase, which terminate at the fcc grain boundaries, while those close to <100> orientation parallel to the tensile direction, marked with M, show no obvious phase transformation or twinning but mainly slip deformation. For the 90° specimen, the grains marked with N with near <111> orientation undergo phase transformation earlier than the others, as shown in Fig. 10.

In the current LPBF-built iHEAs, a large amount of grains close to the <110> orientation aligned with the building direction were generated, forming a <110> growth texture. Meanwhile, as shown in the PFs in Figs. 2c and 2f, those orientations perpendicular to the <110> direction (such as <100>, <011>, but not <111>) are mainly located in the X-Y plane with a relatively concentrated distribution. While for the 90° specimen, due to its relatively weak texture intensity, <111> oriented grains can also be detected on the X-Y plane. Therefore, the <110> growth texture affects the correlation between grain orientations and the loading direction, leading to a weakening of the degree of phase transformation in the 0° specimen relative to that in the 90° specimen despite the better plasticity of the former, as reflected by the in-situ HE-SXRD results in Fig. 6. In addition, a coherent grain rotation effect could also be observed from the comparison of the as-printed and deformed IPFs in Fig. 9 and Fig. 10. For the 90° specimen, the epitaxially grown grains with less preferred orientations around the <110> primary orientation rotate and aggregate, resulting in an enhanced <111> texture intensity and a weakened <110> peak in the IPFs of the deformed specimen. In contrast, for the 0° specimen, the <100> primary orientation along the tensile direction shows no apparent change compared to the as-printed state, but an enhanced <111> peak could be observed after deformation, forming a <100>-<111> double-fiber deformation texture despite the weaker <111> intensity. Similar deformation behavior has also been reported in LPBF-built TWIP steels [32,51] and CoCrFeMnNi-based HEAs [20,52]. In fcc metals, {111} <110> slip is known to occur during deformation, and the activation of this deformation behavior leads to the evolution of initially randomly oriented grains towards a predominant <111>// loading direction and a secondary component close to <100>// loading direction. That is, grains with initial orientations other than <100> will rotate until their respective <111> orientations are aligned with the loading direction, while grains with <100> orientation will remain unchanged during deformation [20,49,50]. This effect becomes more pronounced with increasing strain. Simultaneously, the slip of grains with orientations that favor the gliding of {111} <110> slip systems (such as <111> and <112>) in the current metastable iHEA is accompanied by the formation of hcp phase, resulting in the preferential orientations of $<2\bar{1}\bar{1}2>$hcp and $<10\bar{1}1>$hcp // loading direction for the 0° and 90°

specimens, respectively. During the large deformation stage, the hcp undergoes slip deformation, as represented by the shift and/or decrease in the intensity of the poles close to the above-mentioned preferred orientations during this period. Compared with the relatively uniform distribution of lamellar hcp grains in the 0° specimen, the morphology and distribution of the hcp phase in the 90° specimen are more diverse. At 30 % strain, in addition to the lamellar hcp, there is also the transformation of the hcp domains from aggregates into blocks. The above analysis results once again prove that the grain orientation has a significant impact on the deformation behavior of LPBF-built HEAs.

3.3. Deformation mechanism analysis

The microstructure near the fracture region was characterized by EBSD and TEM to better understand the deformation mechanisms of LPBF-built $Fe_{49.5}Mn_{30}Co_{10}Cr_{10}C_{0.5}$ iHEA. The EBSD results of the 0° and 90° specimens are shown in Fig. 11 and Fig. 12, respectively. A large amount of hcp phase formation can be observed near the fracture region in both specimens (Fig. 11a$_2$ and 12a$_2$). The fcc/hcp interfaces act as obstacles that glissile dislocations have to overcome during plastic deformation [6–8]. Therefore, even at the last stage of plastic deformation, higher stress values are still required to overcome the newly formed fcc/hcp phase interfaces, contributing to a further improvement of the tensile strength of the iHEA, which is consistent with the tensile results in Fig. 5. Fig. 11a$_3$, 11a$_4$, and Fig. 12a$_3$, 12a$_4$ are the complementary IPF maps of fcc and hcp phase near the fracture region of the 0° and 90° specimens, respectively. Significantly different grain morphologies can be observed in these two orientated specimens. That is, the grains of the 90° specimen are greatly elongated, as the long axis of the grains on the X-Y plane is approximately parallel to the tensile direction (Fig. 10), while the short axis of the grains of the 0° specimen is aligned with the loading direction (Fig. 9), resulting in the formation of irregular shaped grains on the X-Y plane. In addition, the hcp phase generated by the deformation-induced phase transformation also shows a clear preferential orientation. EBSD analysis allows establishing a local orientation relationship between the texture and the fcc-hcp transformation. Fig. 11a$_5$ and Fig. 12a$_5$ show the PFs obtained from the partial enlargement of the 0° and 90° specimens, respectively, which demonstrate an obvious orientation relationship of $[1\bar{1}0]$fcc//$[11\bar{2}0]$ hcp and (111)fcc//(0001)hcp in both specimens, reflecting the well-known Shoji-Nishiyama (S-N) orientation relationship in austenitic steels [53].

Furthermore, in addition to the above-mentioned remarkable fcc to hcp phase transformation, obvious slip bands can be observed on the EBSD image quality maps near the fracture region (Fig. 11a$_1$ and Fig. 12a$_1$), confirming the dislocation slip deformation mechanism. Last but not least, both fcc and hcp twin boundaries can be detected in these two specimens, as marked by solid red and green lines in the image quality maps, respectively. The locally enlarged images of the twinning region of the 0° specimen are shown in Figs. 11b and 11c. Σ3 twinning on the {111}fcc planes and the tensile twinning on the {10$\bar{1}$2}hcp planes were separately determined by the analysis of the PF and the misorientation angle. The same twinning systems were also detected in the 90° specimen, as shown in Figs. 12b and 12c. Although these thin twin lamellas had a small volume, unlike conventional TWIP alloys that rely on large-scale mechanical twinning deformation, they were detected in both oriented specimens, indicating the simultaneous development of fcc to hcp phase transformation and twinning in the later deformation stage, which greatly contributes to the strain hardening capability through introducing the dynamic Hall-Petch effect [6–8].

The TEM analyses of the deformed specimen are shown in Fig. 13, revealing more detailed deformation behavior at the nanoscale level. It should be mentioned that since the deformation mechanisms observed in the two oriented specimens are similar, and the TEM analysis area is only of a few square microns, only the results of the 0° specimen are
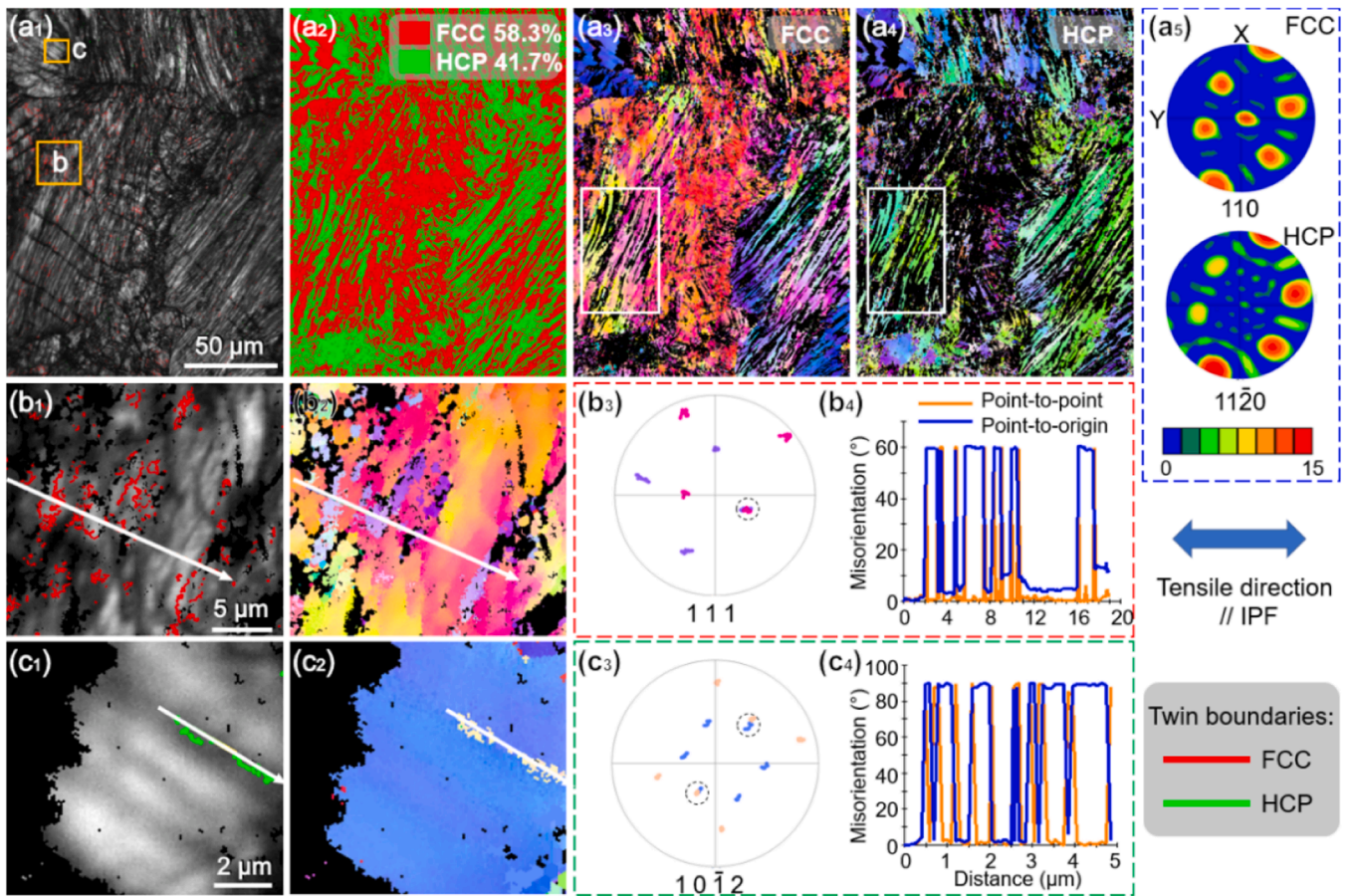
Fig. 11. Post-deformation EBSD results near the fracture area of the 0° specimen: (a₁) image quality map, (a₂) phase map, complementary IPF maps of (a₃) fcc and (a₄) hcp phase, (a₅) PFs obtained from the partial enlargement in (a₃, a₄), (b₁-b₄) twins within a fcc grain and (c₁-c₄) twins within a hcp grain.

shown here as these would be similar between both conditions. In the overview of the dark-field STEM image in Fig. 13a, a high density of slip bands and multiple activated slip systems are observed. Despite considerable deformation, no significant changes in the shape or size of the precipitates were observed, as indicated by the white arrows in Fig. 13a. A local enlarged view of the deformed region is shown in Fig. 13b, where extensive deformation-induced ε-martensite phase and SFs (yellow arrows) are observed. Due to the low SFE of the currently studied iHEA, a unit dislocation with $1/2 < 110 >$ Burgers vector tends to dissociate into two Shockley partial dislocations with $1/6 <\bar{2}11 >$ Burgers vector connected by a SF in a {111} glide plane. Either deformation twining or fcc-hcp martensitic transformation is proceeded by the movement of Shockley partials. When the Shockley partials glide on every second {111} plane, fcc-hcp phase transformation will be generated, while deformation twins will be formed when the Shockley partials glide on every {111} plane [23,54]. During deformation of the current iHEA, dislocation slip is highly localized on pre-existing and strain-induced SFs on differently oriented {111} planes, and these regions mainly evolve into different variants of deformation-induced hcp phase. In Fig. 13c, both primary and secondary hcp phase were captured by HRTEM, and the measured misorientation angle between these two crystallographic variants is about 70.5°, which coincides with the angle between differently oriented {111} planes in the fcc parent phase. The selected area electron diffraction (SAED) (Fig. 13f) from this area confirms the deformation features described above. The detailed S-N orientation relationship ((111)fcc// (0001)hcp, [1$\bar{1}$0]fcc// [11$\bar{2}$0]hcp) and atomic structures of the fcc and hcp phases can be observed in Fig. 13d, consistent with the EBSD results.

Furthermore, nanoscale Σ3 deformation twins can be identified in

Fig. 13e. This confirms the simultaneous existence of TRIP and TWIP effects in this LPBF-built iHEA during tensile deformation. In general, along with plastic strain and dislocation activity, deformation twinning and phase transformation play an increasingly important role in regulating plasticity to maintain a steady strain hardening capability at high strain levels [5]. A large number of SFs can be observed in the primary hcp phase in Fig. 13g, resulting from the remaining local fcc-type stacking formed by irregular slip of Shockley partials not necessarily taking place on every second {111} plane, and such SFs can be eliminated by the movement of Shockley partials [39]. Fig. 13h shows that SFs with different orientations are also formed in the fcc matrix. The interactions of SFs, i.e. Shockley partials gliding on differently oriented {111} planes, generate immobile L-C locks, which not only hinder the movement of the SFs forming them, but also act as obstacles for further gliding from the opposite direction [55,56]. Generally, low SFE in materials will result in a high probability for the formation of L-C locks [55–57]. Due to their extraordinary dislocation accumulation ability, L-C locks can also play an important role in improving strain hardening [55]. Meanwhile, the intersection of these SFs subdivides the matrix into increasingly smaller blocks, achieving a dynamic grain refinement effect. Fig. 13i is the corresponding HRTEM image, which reveals that the misorientation angle between SFs is also 70.5°, consistent with the angle between the above-mentioned hcp variants and also the angle between the two twins commonly found in single crystals of fcc-structured HEAs [3,58], indicating that the current materials tend to activate the secondary phase transformation or twinning systems at higher strain levels.
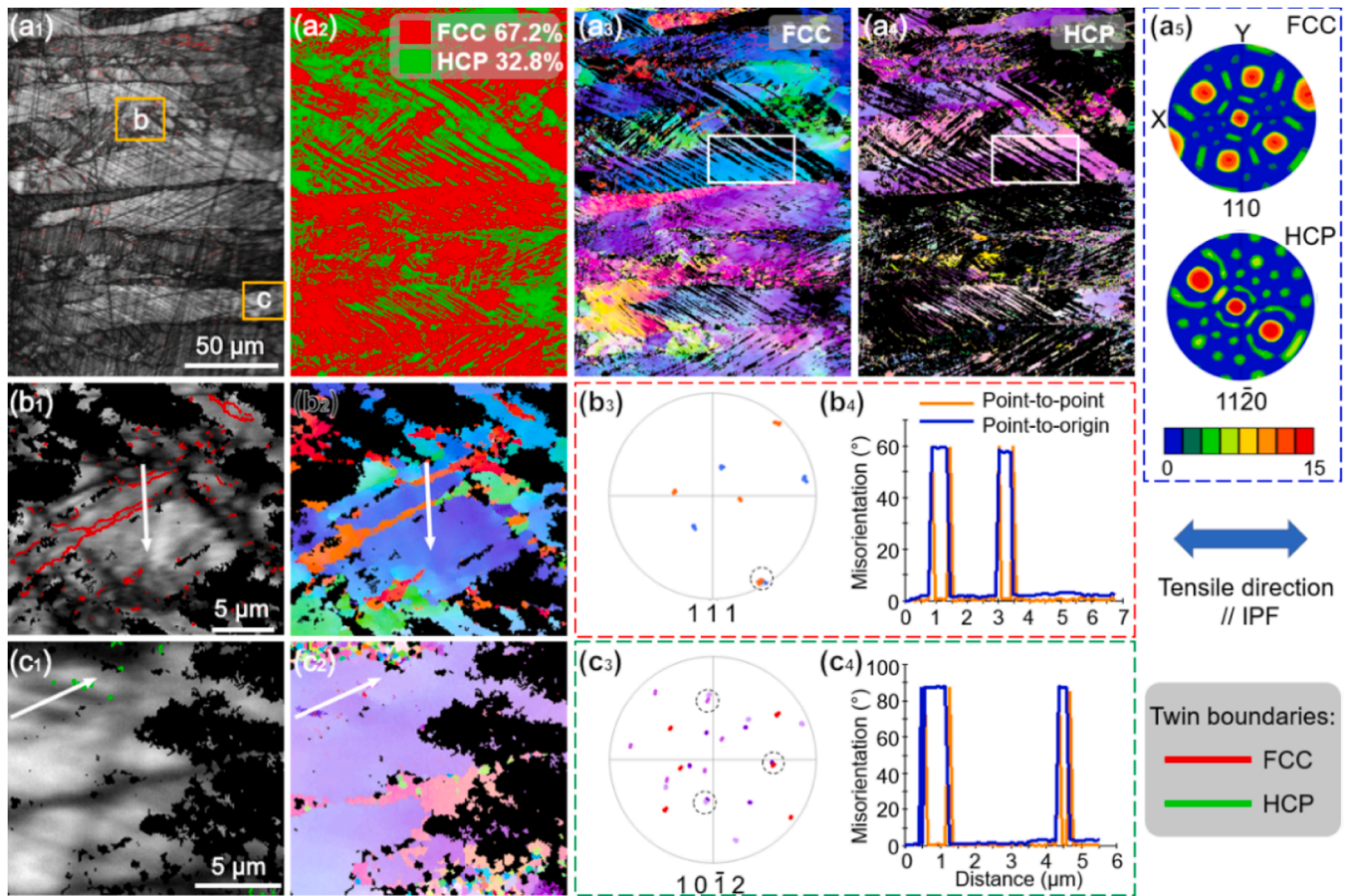
Fig. 12. Post-deformation EBSD results near the fracture area of the 90° specimen: (a₁) image quality map, (a₂) phase map, complementary IPF maps of (a₃) fcc and (a₄) hcp phase, (a₅) PFs obtained from the partial enlargement in (a₃, a₄), (b₁-b₄) twins within a fcc grain and (c₁-c₄) twins within a hcp grain.

4. Conclusions

In this work, two types of $Fe_{49.5}Mn_{30}Co_{10}Cr_{10}C_{0.5}$ iHEA tensile specimens oriented at 0° and 90° relative to the laser scanning direction were prepared by LPBF. The microstructure, mechanical behavior and deformation mechanisms during tensile loading were systematically characterized by SEM, EBSD, S/TEM, in-situ HE-SXRD tensile test and in-situ EBSD analysis. The following conclusions can be drawn:

(1) The as-built $Fe_{49.5}Mn_{30}Co_{10}Cr_{10}C_{0.5}$ iHEA specimens are dominated by fcc phase structure. A complex heterogeneous microstructure consisting of coarse columnar grains, subgrains, high-density dislocation walls, and nano precipitates was observed. The as-built microstructure exhibits a pronounced $<110>$ growth texture parallel to the building direction.

(2) The continuous and steady strain hardening response observed during tensile testing of both types of iHEA specimens originates from the synergistic effect of the massive dislocation networks and the twin/phase boundaries. Hence, superior tensile properties with remarkably improved strength-ductility trade-off of the alloy were achieved. The tensile strength and elongation of the 0° and 90° specimens at room temperature reached 935 MPa, 45 % and 1091 MPa, 35 %, respectively.

(3) In-situ HE-SXRD tensile testing revealed the precise onset of the strain-induced hcp phase transformation. Its volume fraction increases with increasing strain. Moreover, the hcp phase fraction at the fracture strain in the 0° specimen is lower than that of the 90° specimen, originating from the $<110>$ growth texture in

the as-printed specimens, which leads to different preferential grain orientations parallel to the tensile direction.

(4) During deformation, the dominant $<100>$ and weaker $<111>$ preferential orientations parallel to the tensile direction developed in the 0° specimen, while the dominant $<111>$ preferred orientation developed in the 90° specimen. The fcc and hcp produced by the strain-induced phase transformation exhibits a typical Shoji-Nishiyama orientation relationship. Furthermore, post-deformation EBSD and TEM analyses revealed the generation of nanosized twins in the fractured specimens, confirming the simultaneous activation of TWIP and TRIP effects.

CRediT authorship contribution statement

Wei Zhang: Funding acquisition, Conceptualization, Methodology, Investigation, Data curation, Formal analysis, Visualization, Validation, Writing – original draft. **Jiajia Shen**: Data curation, Investigation, Formal analysis, Writing – review & editing. **João P. Oliveira**: Investigation, Writing – review & editing. **Hui Wang**: Data curation, Formal analysis. **Shaochuan Feng**: Investigation, Methodology, Writing – review & editing. **Norbert Schell**: Resources. **Bart J. Kooi**: Supervision, Formal analysis, Writing – review & editing. **Yutao Pei**: Funding acquisition, Conceptualization, Methodology, Supervision, Formal analysis, Writing – review & editing.

Declaration of Competing Interest

The authors declare that they have no known competing financial
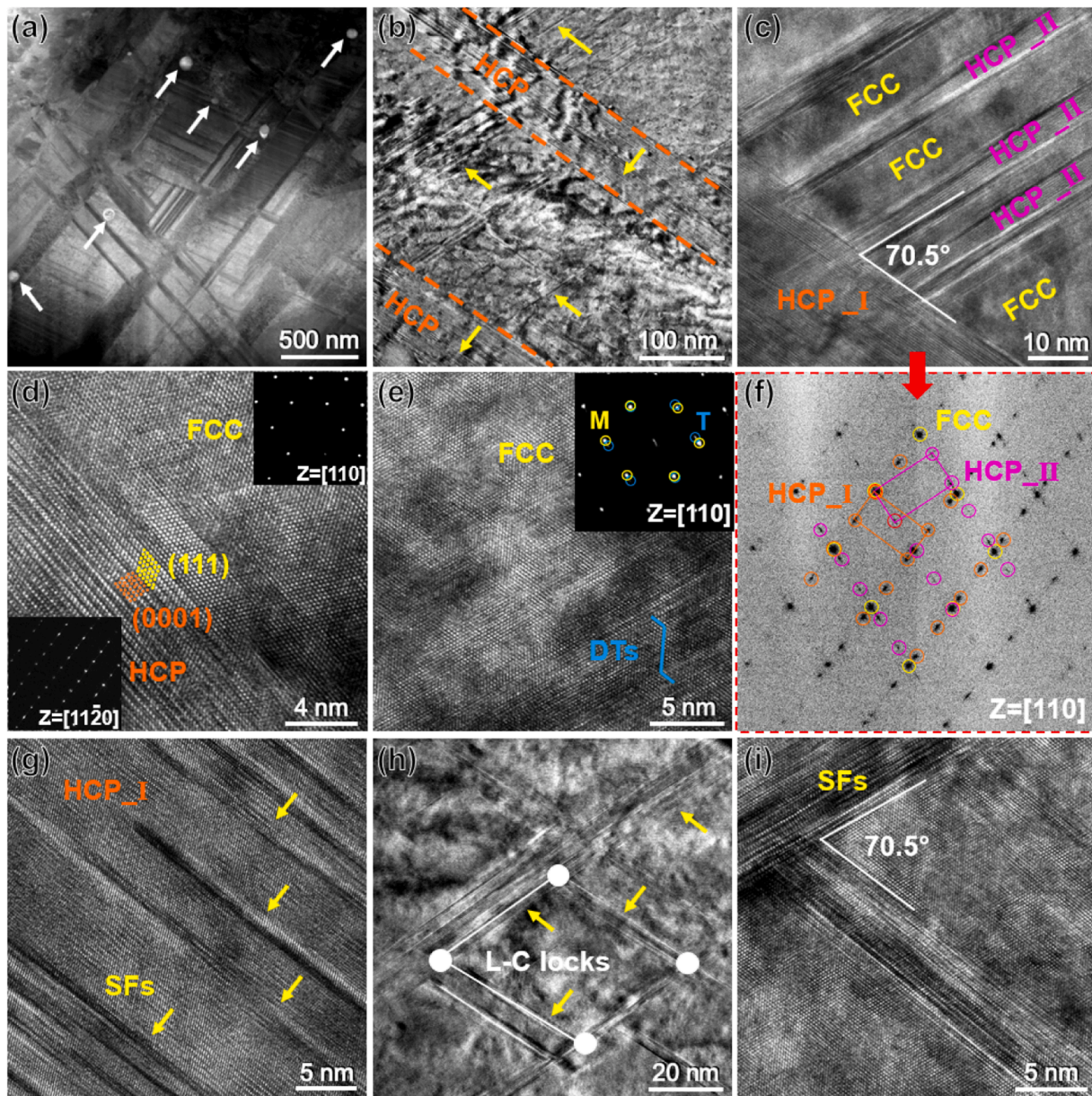
Fig. 13. TEM observations near the fracture area. (a) Overview dark-field STEM image of the deformed specimen, (b) TEM bright-field image of the deformed region, (c) HRTEM image indicates the coexistence of fcc and hcp phases, (d) HRTEM image of the fcc and hcp structure showing the orientation relationship, (e) HRTEM image and the corresponding SAED pattern shows the existence of deformation twins in the fcc matrix, (f) SAED pattern from (c) along [110] zone axis demonstrating the hcp variants, (g) multiple SFs on the strain-induced hcp phase, (h) Lomer-Cottrell locks in the fcc matrix and (i) the corresponding HRTEM image.

interests or personal relationships that could have appeared to influence the work reported in this paper.

Data availability

Data will be made available on request.

Appendix A. Supporting information

Supplementary data associated with this article can be found in the online version at doi:10.1016/j.addma.2023.103791.

References

[1] D.B. Miracle, O.N. Senkov, A critical review of high entropy alloys and related concepts, Acta Mater. 122 (2017) 448–511.

[2] W. Zhang, A. Chabok, B.J. Kooi, Y. Pei, Additive manufactured high entropy alloys: a review of the microstructure and properties, Mater. Des. 220 (2022), 110875.

[3] J. Su, X. Wu, D. Raabe, Z. Li, Deformation-driven bidirectional transformation promotes bulk nanostructure formation in a metastable interstitial high entropy alloy, Acta Mater. 167 (2019) 23–39.

[4] S. Zhu, D. Yan, K. Gan, W. Lu, Z. Li, Awakening the metastability of an interstitial high entropy alloy via severe deformation, Scr. Mater. 191 (2021) 96–100.

[5] Z.G. Zhu, X.H. An, W.J. Lu, Z.M. Li, F.L. Ng, X.Z. Liao, U. Ramamurty, S.M.L. Nai, J. Wei, Selective laser melting enabling the hierarchically heterogeneous microstructure and excellent mechanical properties in an interstitial solute strengthened high entropy alloy, Mater. Res. Lett. 7 (11) (2019) 453–459.

[6] S. Huang, H. Huang, W. Li, D. Kim, S. Lu, X. Li, E. Holmstrom, S.K. Kwon, L. Vitos, Twinning in metastable high-entropy alloys, Nat. Commun. 9 (1) (2018), 2381.

[7] W.R. Jian, Z. Xie, S. Xu, Y. Su, X. Yao, I.J. Beyerlein, Effects of lattice distortion and chemical short-range order on the mechanisms of deformation in medium entropy alloy CoCrNi, Acta Mater. 199 (2020) 352–369.

[8] M. Arul Kumar, B. Clausen, L. Capolungo, R.J. McCabe, W. Liu, J.Z. Tischler, C. N. Tomé, Deformation twinning and grain partitioning in a hexagonal close-packed magnesium alloy, Nat. Commun. 9 (1) (2018), 4761.

[9] Y.H. Zhang, Y. Zhuang, A. Hu, J.J. Kai, C.T. Liu, The origin of negative stacking fault energies and nano-twin formation in face-centered cubic high entropy alloys, Scr. Mater. 130 (2017) 96–99.

[10] W. Zhang, J. Shen, J.P. Oliveira, B.J. Kooi, Y. Pei, Crystallographic orientation-dependent deformation characteristics of additive manufactured interstitial-strengthened high entropy alloys, Scr. Mater. 222 (2023), 115049.

[11] Z. Li, C.C. Tasan, H. Springer, B. Gault, D. Raabe, Interstitial atoms enable joint twinning and transformation induced plasticity in strong and ductile high-entropy alloys, Sci. Rep. 7 (2017) 40704.

[12] D.G. Shaysultanov, K.Sh. Raimov, N.D.. Stepanov, Effect of carbon content, deformation and annealing on the structure and properties of interstitial TRIP high-entropy alloys, IOP Conference Series: Materials Science and Engineering 1014 (2021) 012052.

[13] H. Bikas, P. Stavropoulos, G. Chryssolouris, Additive manufacturing methods and modelling approaches: a critical review, Int. J. Adv. Manuf. Technol. 83 (1) (2016) 389–405.

[14] J.M. Vallejos, P. Barriobero-Vila, J. Gussone, J. Haubrich, K. Kelm, A. Stark, G. Requena, In situ high-energy synchrotron X-ray diffraction reveals the role of texture on the activation of slip and twinning during deformation of laser powder bed fusion Ti-6Al4V, Adv. Eng. Mater. 23 (11) (2021), 2001556.

[15] D. Gu, Y.C. Hagedorn, W. Meiners, G. Meng, R.J.S. Batista, K. Wissenbach, R. Poprawe, Densification behavior, microstructure evolution, and wear performance of selective laser melting processed commercially pure titanium, Acta Mater. 60 (9) (2012) 3849–3860.

[16] Y. Kok, X.P. Tan, P. Wang, M.L.S. Nai, N.H. Loh, E. Liu, S.B. Tor, Anisotropy and heterogeneity of microstructure and mechanical properties in metal additive manufacturing: a critical review, Mater. Des. 139 (2018) 565–586.

[17] P. Barriobero-Vila, R. Jerez-Mesa, A. Guitar, O. Gavalda-Diaz, J.A. Travieso-Rodríguez, A. Stark, J.J. Roa, Deformation kinetics of a TRIP steel determined by in situ high-energy synchrotron X-ray diffraction, Materialia 20 (2021), 101251.

[18] P. Barriobero-Vila, K. Artzt, A. Stark, N. Schell, M. Siggel, J. Gussone, J. Haubrich, Mapping the geometry of Ti-6Al-4V: from martensite decomposition to localized spheroidization during selective laser melting, Scr. Mater. 182 (2020) 48–52.

[19] P. Barriobero-Vila, J. Gussone, K. Kelm, J. Haubrich, A. Stark, N. Schell, G. Requena, An in situ investigation of the deformation mechanisms in a β-quenched Ti-5Al-5V–5Mo-3Cr alloy, Mater. Sci. Eng.: A 717 (2018) 134–143.

[20] B. Han, C. Zhang, K. Feng, Z. Li, X. Zhang, Y. Shen, X. Wang, H. Kokawa, R. Li, Z. Wang, P.K. Chu, Additively manufactured high strength and ductility CrCoNi medium entropy alloy with hierarchical microstructure, Mater. Sci. Eng.: A 820 (2021), 141545.

[21] P. Niu, R. Li, Z. Fan, T. Yuan, Z. Zhang, Additive manufacturing of TRIP-assisted dual-phases Fe50Mn30Co10Cr10 high-entropy alloy: microstructure evolution, mechanical properties and deformation mechanisms, Mater. Sci. Eng.: A 814 (2021), 141264.

[22] Z. Li, K.G. Pradeep, Y. Deng, D. Raabe, C.C. Tasan, Metastable high-entropy dual-phase alloys overcome the strength-ductility trade-off, Nature 534 (7606) (2016) 227–230.

[23] D. Wei, X. Li, J. Jiang, W. Heng, Y. Koizumi, W.M. Choi, B.J. Lee, H.S. Kim, H. Kato, A. Chiba, Novel Co-rich high performance twinning-induced plasticity (TWIP) and transformation-induced plasticity (TRIP) high-entropy alloys, Scr. Mater. 165 (2019) 39–43.

[24] J.M. Park, J. Choe, J.G. Kim, J.W. Bae, J. Moon, S. Yang, K.T. Kim, J.H. Yu, H. S. Kim, Superior tensile properties of 1%C-CoCrFeMnNi high-entropy alloy additively manufactured by selective laser melting, Mater. Res. Lett. 8 (2019) 1638844.

[25] O. Andreau, I. Koutiri, P. Peyre, J.-D. Penot, N. Saintier, E. Pessard, T.D. Terris, C. Dupuy, T. Baudin, Texture control of 316L parts by modulation of the melt pool morphology in selective laser melting, J. Materrials Process. Technol. 264 (2019) 21–31.

[26] J.J. Marattukalam, D. Karlsson, V. Pacheco, P. Beran, U. Wiklund, U. Jansson, B. Hjörvarsson, M. Sahlberg, The effect of laser scanning strategies on texture, mechanical properties, and site-specific grain orientation in selective laser melted 316L SS, Mater. Des. 193 (2020), 108852.

[27] K.M. Bertsch, G. Meric de Bellefon, B. Kuehl, D.J. Thoma, Origin of dislocation structures in an additively manufactured austenitic stainless steel 316L, Acta Mater. 199 (2020) 19–33.

[28] R. Li, P. Niu, T. Yuan, P. Cao, C. Chen, K. Zhou, Selective laser melting of an equiatomic CoCrFeMnNi high-entropy alloy: processability, non-equilibrium microstructure and mechanical property, J. Alloy. Compd. 746 (2018) 125–134.

[29] Y.M. Wang, T. Voisin, J.T. McKeown, J. Ye, N.P. Calta, Z. Li, T. Zhu, Additively manufactured hierarchical stainless steels with high strength and ductility, Nat. Mater. 17 (1) (2018) 63–71.

[30] L. Liu, Q. Ding, Y. Zhong, J. Zou, J. Wu, Y.L. Chiu, Z. Shen, Dislocation network in additive manufactured steel breaks strength–ductility trade-off, Mater. Today 21 (4) (2018) 354–361.

[31] J.G. Kim, J.M. Park, J.B. Seol, J. Choe, J.-H. Yu, S. Yang, H.S. Kim, Nano-scale solute heterogeneities in the ultrastrong selectively laser melted carbon-doped CoCrFeMnNi alloy, Mater. Sci. Eng.: A 773 (2020), 138726.

[32] C. Haase, J. Bultmann, J. Hof, S. Ziegler, S. Bremen, C. Hinke, A. Schwedt, U. Prahl, W. Bleck, Exploiting process-related advantages of selective laser melting for the production of high-manganese steel, Materials 10 (1) (2017) 56.

[33] R. Zhou, Y. Liu, B. Liu, J. Li, Q. Fang, Precipitation behavior of selective laser melted FeCoCrNiC0.05 high entropy alloy, Intermetallics 106 (2019) 20–25.

[34] H.T. Lee, C.T. Chen, Numerical and experimental investigation into effect of temperature field on sensitization of AISI 304 in butt welds fabricated by gas tungsten arc welding, Mater. Trans. 52 (7) (2011) 1506–1514.

[35] Z. Wu, C.M. Parish, H. Bei, Nano-twin mediated plasticity in carbon-containing FeNiCoCrMn high entropy alloys, J. Alloy. Compd. 647 (2015) 815–822.

[36] P. Barriobero-Vila, J.M. Vallejos, J. Gussone, J. Haubrich, K. Kelm, A. Stark, N. Schell, G. Requena, Interface-mediated twinning-induced plasticity in a fine hexagonal microstructure generated by additive manufacturing, Adv. Mater. 33 (52) (2021), e2105096.

[37] X.H. Hu, X. Sun, L.G. Hector, Y. Ren, Individual phase constitutive properties of a TRIP980 steel from a combined synchrotron X-ray diffraction and crystal plasticity approach, Acta Mater. 132 (2017) 230–244.

[38] Y. Tong, K. Jin, H. Bei, J.Y.P. Ko, D.C. Pagan, Y. Zhang, F.X. Zhang, Local lattice distortion in NiCoCr, FeCoNiCr and FeCoNiCrMn concentrated alloys investigated by synchrotron X-ray diffraction, Mater. Des. 155 (2018) 1–7.

[39] Y. Koizumi, S. Suzuki, K. Yamanaka, B.S. Lee, K. Sato, Y. Li, A. Chiba, Strain-induced martensitic transformation near twin boundaries in a biomedical Co–Cr–Mo alloy with negative stacking fault energy, Acta Mater. 61 (5) (2013) 1648–1661.

[40] Z. Li, C.C. Tasan, K.G. Pradeep, D. Raabe, A TRIP-assisted dual-phase high-entropy alloy: grain size and phase fraction effects on deformation behavior, Acta Mater. 131 (2017) 323–335.

[41] M. Béreš, C.C. Silva, P.W.C. Sarvezuk, L. Wu, L.H.M. Antunes, A.L. Jardini, A.L. M. Feitosa, J. Žilková, H.F.G. de Abreu, R.M. Filho, Mechanical and phase transformation behaviour of biomedical Co-Cr-Mo alloy fabricated by direct metal laser sintering, Mater. Sci. Eng.: A 714 (2018) 36–42.

[42] L.H.M. Antunes, J.J. Hoyos, E.B. Fonseca, M. Béreš, P.F. da Silva Farina, E.S. N. Lopes, A.L. Jardini, R.M. Filho, Effect of phase transformation on ductility of additively manufactured Co–28Cr–6Mo alloy: an in situ synchrotron X-ray diffraction study during mechanical testing, Mater. Sci. Eng.: A 764 (2019), 138262.

[43] C. Ullrich, S. Martin, C. Schmpf, A. Stark, N. Schell, D. Rafaja, Deformation mechanisms in metastable austenitic TRIP/TWIP steels under compressive load studied by in-situ synchrotron radiation diffraction, Adv. Eng. Mater. 21 (2019) 1801101.

[44] X. Zhang, R. Teng, T. Liu, Y. Shi, Z. Lv, Q. Zhou, X. Wang, Y. Wang, H. Liu, Z. Xing, Improving strength-ductility synergy in medium Mn steel by combining heterogeneous structure and TRIP effect, Mater. Charact. 184 (2022), 111661.

[45] J. Talonen, H. Hänninen, Formation of shear bands and strain-induced martensite during plastic deformation of metastable austenitic stainless steels, Acta Mater. 55 (18) (2007) 6108–6118.

[46] H.K.D.H. Bhadeshia, S.R. Honeycombe, The strengthening of iron and its alloys. Steels, fourth edition.,, Elsevier,, 2006, pp. 17–38, https://doi.org/10.1016/B978-075068084-4/50004-2.

[47] J. Johansson, M. Odén, H. Zhang, Evolution of the residual stress state in a duplex stainless steel during loading, Acta Mater. 47 (1999) 2669–2684.

[48] S. Sato, E.P. Kwon, M. Imafuku, K. Wagatsuma, S. Suzuki, Microstructural characterization of high-manganese austenitic steels with different stacking fault energies, Mater. Charact. 62 (8) (2011) 781–788.

[49] C.E. Slone, S. Chakraborty, J. Miao, E.P. George, M.J. Mills, S.R. Niezgoda, Influence of deformation induced nanoscale twinning and FCC-HCP transformation on hardening and texture development in medium-entropy CrCoNi alloy, Acta Mater. 158 (2018) 38–52.

[50] B. Uzer, S. Picak, J. Liu, T. Jozaghi, D. Canadinc, I. Karaman, Y.I. Chumlyakov, I. Kireeva, On the mechanical response and microstructure evolution of NiCoCr single crystalline medium entropy alloys, Mater. Res. Lett. 6 (8) (2018) 442–449.

[51] T. Niendorf, F. Brenne, Steel showing twinning-induced plasticity processed by selective laser melting – an additively manufactured high performance material, Mater. Charact. 85 (2013) 57–63.

[52] S.H. Joo, H. Kato, M.J. Jang, J. Moon, C.W. Tsai, J.W. Yeh, H.S. Kim, Tensile deformation behavior and deformation twinning of an equimolar CoCrFeMnNi high-entropy alloy, Mater. Sci. Eng.: A 689 (2017) 122–133.

[53] M. Eskandari, A. Zarei-Hanzaki, M.A. Mohtadi-Bonab, Y. Onuki, R. Basu, A. Asghari, J.A. Szpunar, Grain-orientation-dependent of γ-ε-α′ transformation and twinning in a super-high-strength, high ductility austenitic Mn-steel, Mater. Sci. Eng.: A 674 (2016) 514–528.

[54] G.B. Olson, M. Cohen, A general mechanism of martensitic nucleation: Part I. General concepts and the FCC → HCP transformation, Metall. Trans. A 7 (1976) 1897–1904.

[55] D.D. Zhang, J.Y. Zhang, J. Kuang, G. Liu, J. Sun, Superior strength-ductility synergy and strain hardenability of Al/Ta co-doped NiCoCr twinned medium entropy alloy for cryogenic applications, Acta Mater. 220 (2021), 117288.

[56] N. Yao, T. Lu, K. Feng, B. Sun, R.Z. Wang, J. Wang, Y. Xie, P. Zhao, B. Han, X. C. Zhang, S.T. Tu, Ultrastrong and ductile additively manufactured precipitation-hardening medium-entropy alloy at ambient and cryogenic temperatures, Acta Mater. 236 (2022), 118142.

[57] P. Shi, Y. Zhong, Y. Li, W. Ren, T. Zheng, Z. Shen, B. Yang, J. Peng, P. Hu, Y. Zhang, P.K. Liaw, Y. Zhu, Multistage work hardening assisted by multi-type twinning in ultrafine-grained heterostructural eutectic high-entropy alloys, Mater. Today 41 (2020) 62–71.

[58] J.Y. He, Q. Wang, H.S. Zhang, L.H. Dai, T. Mukai, Y. Wu, X.J. Liu, H. Wang, T. G. Nieh, Z.P. Lu, Dynamic deformation behavior of a face-centered cubic FeCoNiCrMn HEA, Sci. Bull. 63 (6) (2018) 362–368.